SPE-212635-MS

An Efficient Simulation Approach for Long-term Assessment of CO2 Storage in Complex Geological Formations

Ziliang Zhang, Department of Applied Mathematics, Delft University of Technology; Yuhang Wang, Department of Geosciences and Engineering, Delft University of Technology; Cornelis Vuik, Department of Applied Mathematics, Delft University of Technology; Hadi Hajibeygi, Department of Geosciences and Engineering, Delft University of Technology

 DOI 10.2118/212635-MS

This paper was prepared for presentation at the SPE Reservoir Characterisation and Simulation Conference and Exhibition held in Abu Dhabi, UAE, 24 - 26 January 2023.

Abstract

We present an efficient compositional framework for simulation of CO2 storage in saline aquifers with complex geological geometries during a lifelong injection and migration process. To improve the computation efficiency, the general framework considers the essential hydrodynamic physics, including hysteresis, dissolution and capillarity, by means of parameterized space. The parameterization method translates physical models into parameterized spaces during an offline stage before simulation starts. Among them, the hysteresis behavior of constitutive relations is captured by the surfaces created from bounding and scanning curves, on which relative permeability and capillarity pressure are determined directly with a pair of saturation and turning point values. The new development also allows for simulation of realistic reservoir models with complex geological features. The numerical framework is validated by comparing simulation results obtained from the Cartesian-box and the converted corner-point grids of the same geometry, and it is applied to a field-scale reservoir eventually. For the benchmark problem, the CO2 is injected into a layered formation. Key processes such as accumulation of CO2 under capillarity barriers, gas breakthrough and dissolution, are well captured and agree with the results reported in literature. The roles of various physical effects and their interactions in CO2 trapping are investigated in a realistic reservoir model using the corner-point grid. It is found that dissolution of CO2 in brine occurs when CO2 and brine are in contact. The effect of residual saturation and hysteresis behavior can be captured by the proposed scanning curve surface in a robust way. The existence of capillarity causes less sharp CO2-brine interfaces by enhancing the imbibition of the brine behind the CO2 plume, which also increases the residual trapping. Moreover, the time-dependent characteristics of the trapping amount reveals the different time scales on which various trapping mechanisms (dissolution and residual) operate and the interplay. The novelty of the development is that essential physics for CO2 trapping are considered by the means of parameterized space. As it is implemented on corner-point grid geometries, it casts a promising approach to predict the migration of CO2 plume, and to assess the amount of CO2 trapped by different trapping mechanisms in realistic field-scale reservoirs.

Introduction

Carbon dioxide capture and storage (CCS) has been widely recognized as a straightforward solution to reduce greenhouse gas emissions (Metz et al., 2005). In this strategy, CO2 emissions from large-point source emitters, such as power plants and factories, are collected and transported to storage sites. Next, CO2 is injected into a secure geological container, which has an impermeable unit above as the caprock and a porous unit as the reservoir to store CO2 successfully (Cooper 2009). Among possible geological storage formations, saline aquifer is one of the promising sites because of its prevalence in sedimentary basins. In this case, the flowing fluids are composed of CO2 and brine primarily. Because of their contrast in physical properties, as well as interactions between different phases, such a displacement process is highly unstable, which leads to various trapping mechanisms.

The trapping mechanisms, by which the injected CO2 is securely trapped in saline aquifers, have been well recognized, including structural and stratigraphic trapping, residual trapping, solubility trapping (Duan et al., 2003; Spycher et al., 2003), and mineral trapping (Emami-Meybodi et al., 2015; Wang et al., 2022). For more detailed information, readers are referred to Metz et al. (2005). Although these trapping mechanisms are clearly classified, the time scales on which different mechanisms operate are not separated and might overlap with each other. Understanding the interplay between different trapping mechanisms remains to be a challenging task. To address this, it is necessary to develop an efficient simulator that captures those essential trapping mechanisms in a unified framework.

In this work, a numerical model is developed to investigate CO2 storage in saline aquifers with complex geological geometries. The underlying physics, including hysteresis, dissolution, and capillarity, are accounted for in a unified compositional framework. In particular, the hysteresis effect is described in a parameterized space to improve the computational efficiency. Moreover, the compositional framework is extended to corner-point grids, which is the industry standard to present subsurface media with complex geological features. This is a significant step towards applying the proposed compositional framework to field-scale applications.

This work is structured as follows. Firstly, the governing equations describing the CO2-brine system, the discretization scheme, and the solution strategy are presented. Following that, incorporation of the physical models into the compositional formulation is addressed. In Section 4, implementation of corner-point grids is validated. In Section 5, simulation results for a field-scale model with lifelong assessment of trapping behavior are presented. Moreover, the roles of different physics and their impacts on the trapping are discussed. Key findings are summarized at the end.

Methodology

Governing equation

Mass conservation law describes the flow and transport of a multicomponent multiphase system in porous media, which reads

$$\frac{\partial}{\partial t}\left(\phi\sum_{\alpha=1}^{n_{ph}} x_{c,\alpha}\rho_\alpha S_\alpha\right)+\nabla\cdot\left(\sum_{\alpha=1}^{n_{ph}} x_{c,\alpha}\rho_\alpha u_\alpha\right)-\sum_{\alpha=1}^{n_{ph}} x_{c,\alpha}\rho_\alpha q_\alpha = 0, \quad \forall\, c\in\{1, \quad ., n_c\}$$

Here, α and c represent the fluid phases and components. Specifically in our case, the two components, CO2 and brine exist in liquid and gas phases. Moreover, ρ_α, S_α, and q_α are the density, saturation, and flow rate of phase α, respectively. Most importantly, $x_{c,\alpha}$ in all the three terms is the mass fraction of components in phase α, and it distinguishes compositional flow from two-phase flow because components are allowed to be split into different phases. u_α is the phase velocity, which can be described by Darcy's law as

$$u_\alpha = \frac{kk_{r,\alpha}}{\mu_\alpha}\nabla\left(p_\alpha-\rho_\alpha gh\right), \quad \alpha = 1, \quad \ldots, \quad n_{phr}$$

Here, k is the rock permeability, $k_{r,\alpha}$ and μ_α are phase relative permeability, phase viscosity respectively. The pressure difference between different phases is related with capillary pressure as

$$p_\alpha - p_\beta = p_{c\alpha,\beta}, \quad \forall\, \alpha \neq \beta \in \{1, \quad ., n_{ph}\}.$$

In addition, the saturation constraint reads

$$\sum_{\alpha=1}^{n_{ph}} S_\alpha = 1.$$

Thermodynamic equilibrium

When multiple phases are present, it is usually assumed that all phases reach thermodynamic equilibrium to decouple phase behavior calculation from flow and transport (Cusini et al., 2018; Lyu et al., 2021), i.e.,

$$f_{c,\alpha}(p, \quad x_{c,\alpha}) - f_{c,\beta}(p, \quad x_{c,\beta}) = 0, \quad \forall\, \alpha \neq \beta \in \{1, \quad ., n_{ph}\}.$$

Here, $f_{c,\alpha}$ is the fugacity of component c in phase α. The overall fraction of component c, z_c, can be defined as

$$z_c - \sum_{\alpha=1}^{n_{ph}} v_\alpha x_{c,\alpha} = 0, \quad \forall\, c \in \{1, \quad ., n_c\},$$

where v_α is the mole fraction of phase α, which can be expressed as a function of saturation, i.e.,

$$v_\alpha = \frac{S_\alpha \rho_\alpha}{\sum_{\alpha=1}^{n_{ph}} S_\alpha \rho_\alpha}.$$

The phase constraint based on mass fraction term reads

$$\sum_{c=1}^{n_c} x_{c,\alpha} = 1 \quad \alpha = 1, \quad \ldots, \quad n_{ph}$$

Overall-composition formulation

In our two-component and two-phase system, overall composition variable set is chosen to solve the problem, and primary variables include one phase pressure and one overall molar fraction. With the defined overall molar composition, the mass conservation equation for each component states,

$$\frac{\partial}{\partial t}\left(\phi \rho_T z_c\right) + \nabla \cdot \left(\sum_{\alpha=1}^{n_{ph}} x_{c,\alpha} \rho_\alpha u_\alpha\right) - \sum_{\alpha=1}^{n_{ph}} x_{c,\alpha} \rho_\alpha q_\alpha = 0, \quad \forall\, c \in \{CO2, \quad brine\}.$$

Here, ρ_T is total density, which can be computed with phase density and saturation. Voskov et al. (2012) compared the formulations that use different variable sets to solve the isothermal compositional problem. It is found overall composition variable set has the advantage that no variable substitution is needed, or equation and variables are the same for every cell comparing with natural variable set, although phase equilibrium computation cannot be avoided for every grid cell.

Solution strategy

The nonlinear system of equations is solved using a finite volume discretization in space and implicit time discretization scheme, in which properties are evaluated on next timestep. We employ Newton-Raphson method to linearize the system of nonlinear equations using p_l and z_{CO2} as primary variables, which leads to

$$r^{v+1}_{c,\{i\}} \approx r^{v}_{c,\{i\}} + \left.\frac{\partial r^{v}_{c,\{i\}}}{\partial p_l}\right|^{v} \delta p^{v+1}_{l} + \left.\frac{\partial r^{v}_{c,\{i\}}}{\partial z_{CO2}}\right|^{v} \delta z^{v+1}_{CO2} = 0,$$

where v and $v + 1$ are the current and next iteration step respectively. Then the linearized equations can be solved iteratively according to

$$J^{v}\delta x^{v+1} = -r^{v},$$

where J_v and r_v are Jacobian and Residual matrix, while $\delta x_v{}^{+1}$ is the primary variable update. The same function in matrix multiplication form can be stated as

$$\begin{pmatrix} \frac{\partial r_{CO2}}{\partial p_l} & \frac{\partial r_{CO2}}{\partial z_{CO2}} \\ \frac{\partial r_b}{\partial p_l} & \frac{\partial r_b}{\partial z_{CO2}} \end{pmatrix} \begin{pmatrix} \delta p_l \\ \delta z_{CO2} \end{pmatrix} = -\begin{pmatrix} r_{CO2} \\ r_b \end{pmatrix}.$$

This iterative process is repeated until it reaches non-linear convergence, which mathematically means the infinite (or any other) norm of the residual and variable update are less than a certain tolerance. In addition, an adaptive time stepping strategy is employed to reduce the number of iterations needed to reach convergence. In this work, the time step size is dynamically changing between user defined maximum and minimum time step size, based on the number of iterations needed to converge.

Physical models

Dissolution

The solubility of CO2 in brine depends on several physical parameters, including pressure, temperature, and water salinity (Spycher et al., 2003). In this work, at given temperature and salinity, the volume of CO2 that can be dissolved into unit volume of brine, R_s, or the solution CO2-brine ratio gives the amount of CO2 dissolved into brine at different pressure.

We employ the same thermodynamic model in Spycher et al. (2005), Hassanzadeh et al. (2008), and Wang et al. (2022), to predict the solution CO2-brine ratio by equating chemical potentials, i.e.,

$$R_s = \frac{\rho_b^{STC} x_{CO2,l}}{\rho_{CO2}^{STC}\left(1 - x_{CO2,l}\right)}.$$

Here, *STC* denotes standard condition. In our isothermal system, assuming the salinity of brine is constant, the solubility of CO2 is only function of pressure. Thus, the relationship between R_s and pressure can be generated during an offline stage and stored in a lookup table before simulation starts. The R_s value can be directly read from the table with known pressure, as shown in Figure 1.

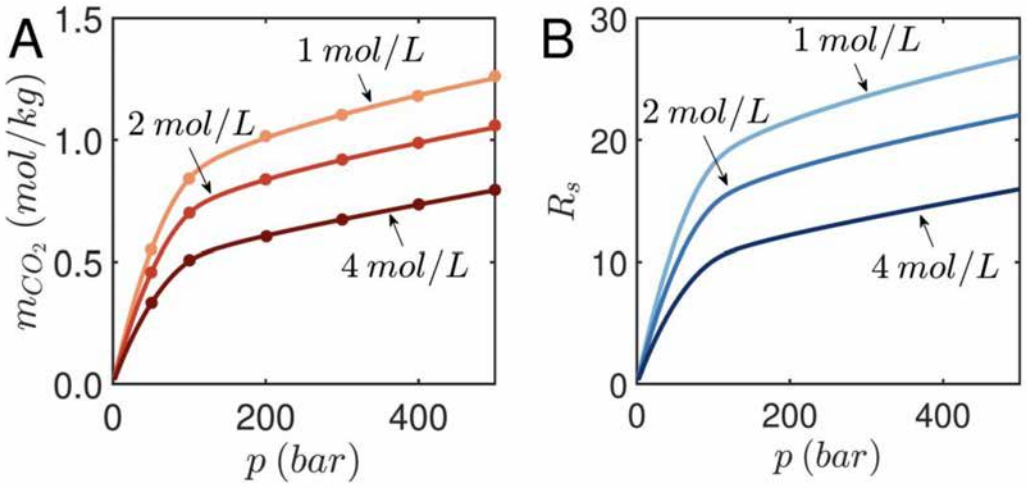

Figure 1—The predication of CO2 solubility in brine at 60 C (Wang et al., 2022).

However, the amount of CO2 present in brine for each reservoir grid also depends on available CO2 in that cell (Hajibeygi et al., 2013). Thus, a stability test is preformed to check the number of phases existing in each cell after the primary variables are updated at each iteration (Wang et al., 2022). For a single-phase cell, CO2 available in that cell is not enough to reach dissolution limit. Thus, if only liquid exits in a cell, the solution CO2-brine ratio is computed based on the overall molar fraction of CO2 as

$$R_s = \frac{\rho_b^{STC} z_{CO2}}{\rho_{CO2}^{STC}(1 - z_{CO2})}.$$

Hysteresis

Hysteresis effect mainly refers to the behavior that different relative permeability or capillary pressure curves are followed during drainage and imbibition process (Juanes et al., 2006). When it comes to field operation, drainage process is happening during injection stage, during which CO2 saturation keeps increasing. The constitutive relations follow the primary drainage curve. After injection stops, the process is often switched to imbibition. It should be noted that the transition from drainage to imbibition process does not always happen at the maximum gas saturation. The drainage process is often interrupted before S_{CO2} reaches its maximum, and changes to imbibition process.

The hysteretic effect in relative permeability and capillary pressure have been captured by experiments (Oak et al., 1990; Pini and Benson, 2017). To ensure the transition is continuous, a series of scanning curves are constructed based on primary bounding curves as shown in Figure 2A (Killough 1976). The scanning curve for each cell is constructed after determining the flow process cell by cell. The determination of the process is based on comparing gas saturation from previous two timesteps, or n and n-1. For example, if $S_g^n < S_g^{n-1}$ on primary drainage curve, it indicates the process is already transitioned to the scanning curve with the turning point given by $S_g^{n-1}(S_{gt})$.

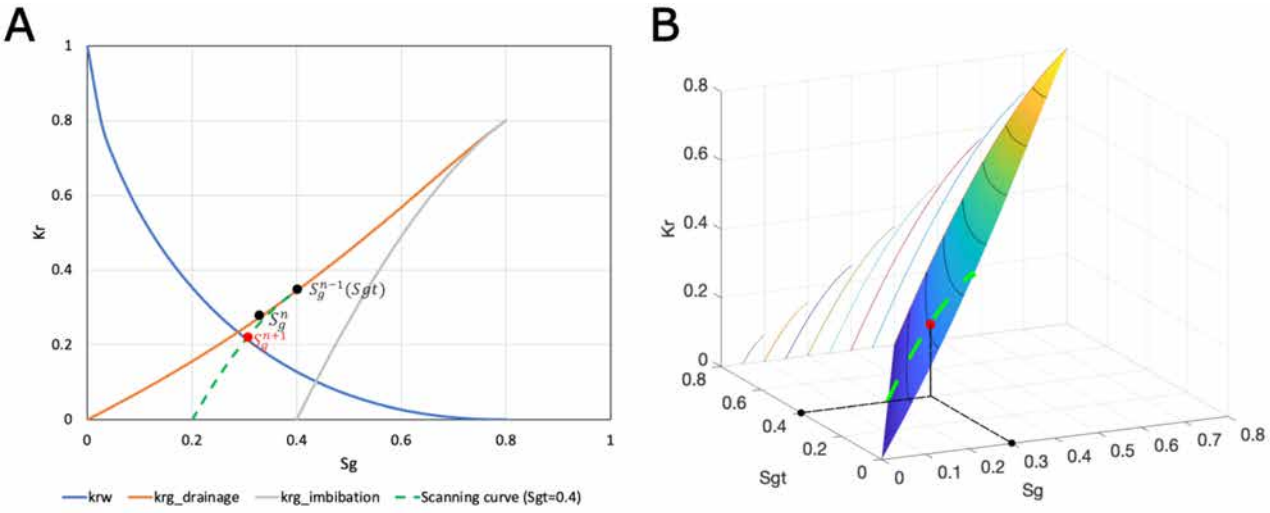

Figure 2—Illustration of hysteretic relative permeability models. (A) Determination process based on scanning curves. (B) Determination process based on the proposed scanning curve surface.

However, this workflow is not computationally efficient because scanning curves are constructed repetitively in each grid. The computational cost increases along with the number of grids. Here we propose a new workflow, in which a scanning curve surface for the constitutive relations is generated at an offline stage. The gas relative permeability or capillary pressure can be readily obtained from the surface knowing the gas saturation and turning point shown in Figure 2B. In this way, we avoid constructing scanning curves repetitively when cells share a same one. Figure 3 illustrates the generated parameterization spaces for relative permeability and capillarity pressure.

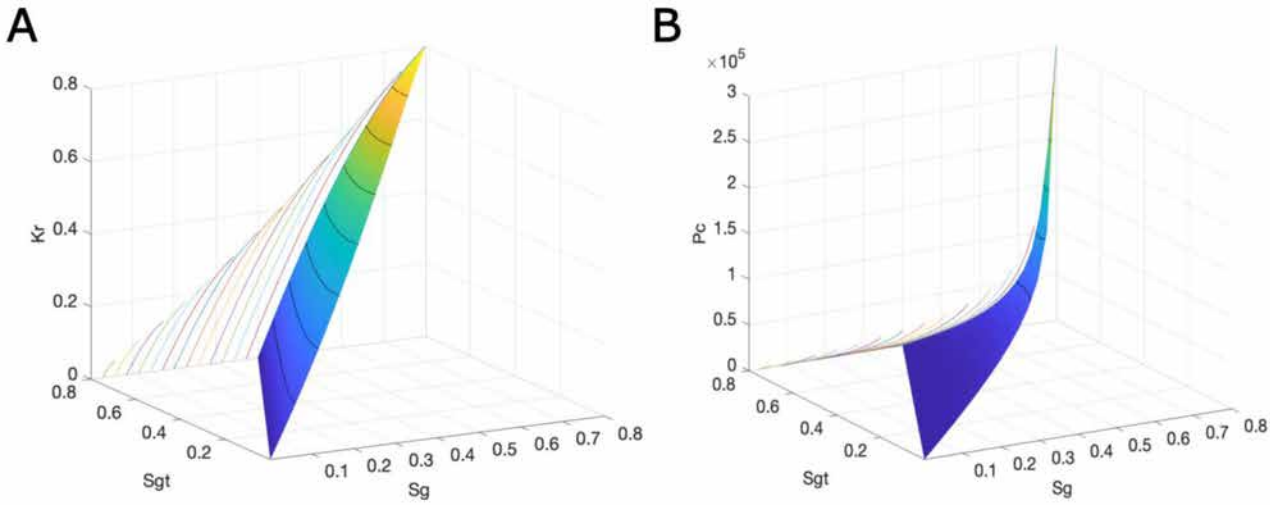

Figure 3—Scanning curve surfaces to model the hysteretic behaviors of relative permeability (A) and capillary pressure (B).

Capillarity

Capillary pressure is defined as pressure difference across the curved interface between non-wetting and wetting phases, and it plays an important role in CO2 storage. For example, capillary pressure in low permeability rock with smaller pore radius is larger than rock with high permeability rock containing the same fluids (Fanchi 2002). CO2 can be collected under or even outside structural and stratigraphic traps at high saturation, when the buoyancy force cannot overcome the capillary forces caused by narrower pore throat of caprock, such that CO2 cannot enter the overlying pore space (Hermanrud et al., 2009). In addition,

a portion of CO2 might be left as discontinuous ganglia and becomes immobilized because of capillary forces. In this work, capillary pressure curves are modelled by the Leverett J-function, as given by Figure 3.

Validation

Layered sand-shale model

The first test case is a benchmark study on CO2 injection into a layered sand-shale aquifer, as shown in Figure 4. Based on the Sleipner Vest CO2 injection project, the 2D test case is designed to investigate key physical processes during CO2 injection in layered formation, such as the viscous to buoyancy-driven flow and CO2 accumulation under capillarity barrier (Pruess et al., 2004; Afanasyev et al., 2016; Shao et al., 2020). With this benchmark study, the physical effects, including dissolution and capillarity, incorporated into our compositional framework are validated.

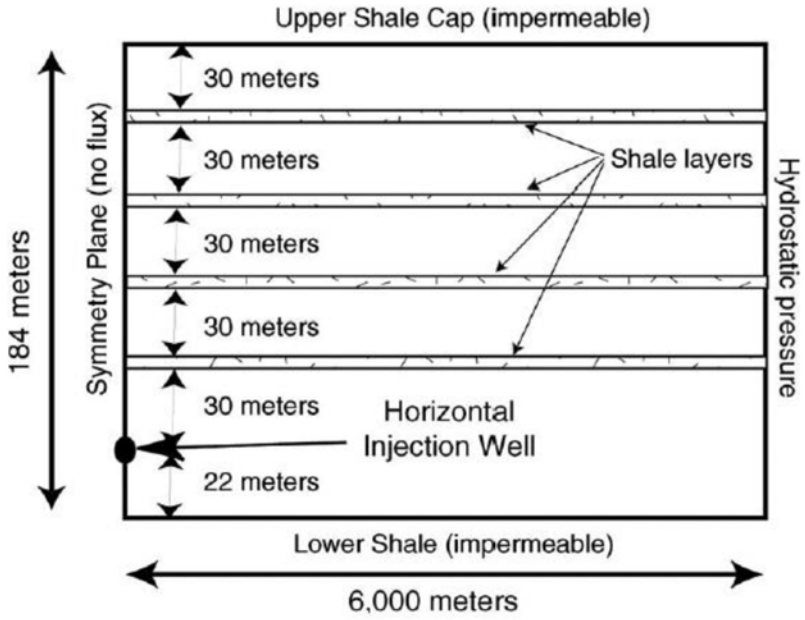

Figure 4—CO2 injection into an idealized layered sand-shale formation

The 2D domain is a vertical plane with a length of 6000 meters and height of 184 meters, and only 1 meter thick cross section perpendicular to the horizontal well is modelled. The geometry of the formation is idealized to consist of 5 sand layers that interbedded with 4 low permeability shale layers. The injection well is 30 meters below the lowest shale layer and there is another 22 meters of sand unit below the well. The reservoir properties for the sand and shale layers are summarized in Table 1. The relative permeability and capillary pressure curve for both sand and shale layers are given by Figure 5.

Table 1—Petrophysical parameters of sand and shale layers

Properties	Symbols	Units	Sand	Shale
Porosity	ϕ	–	0.35	0.1025
Permeability	k	mD	3000	10
Residual gas saturation	S_{rg}	–	0.05	0.05
Residual water saturation	S_{rw}	–	0.20	0.20
Capillary entry pressure	p_{ce}	kPa	3.58	62.00

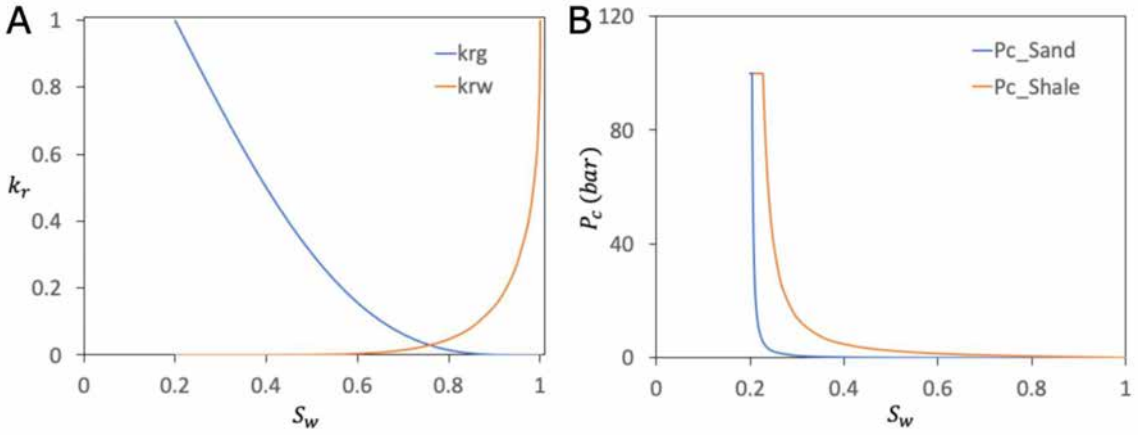

Figure 5—Relative permeability and capillary pressure models for sand and shale layers. (A) Relative permeability for both sand and shale layers. (B) Capillary pressure.

The initial formation temperature is 37 °C and an isothermal condition is assumed. Fluid flow is only allowed at the right boundary, while no mass flux is allowed to across the other three boundaries. The right boundary is fixed at hydrostatic pressure to allow fluid to flow in or out and to avoid over pressurizing the system. The initial pressure at the height where injection well is perforated is about 110 bars.

Figure 6A shows the comparison of gas saturation distribution after 2 years of injection. As CO2 is injected into the aquifer, it tends to flow upward due to the density contrast between CO2 and brine. When the injected CO2 reaches the shale layers, CO2 is accumulated below those capillary barriers because a higher capillary entry pressure needs to be exceeded before CO2 can breakthrough. Since CO2 cannot migrate upward freely, CO2 plume in sand layers below tend to spread and migrate into the aquifer further. The comparison between our simulation results and former research shows good agreement on the distance and the height CO2 plume migrates.

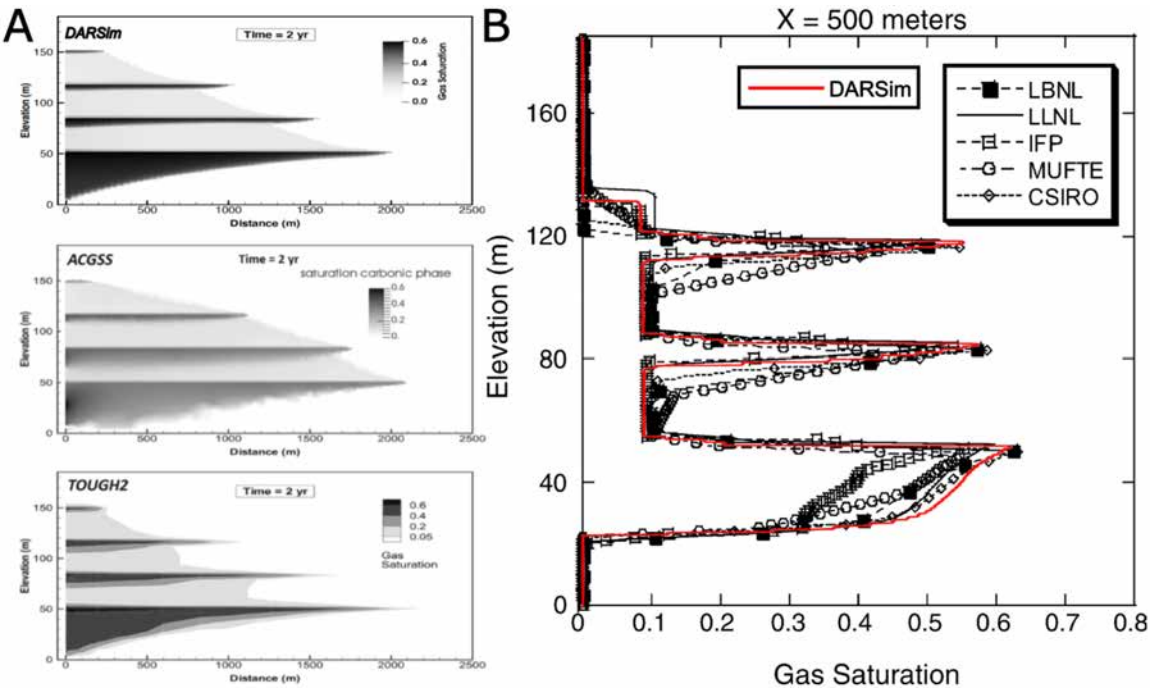

Figure 6—Predicted gas saturation profile after 2 year. (A) In the left of the reservoir: DARSim (top), ACGSS (middle) and TOUGH2 (bottom). (B) Along a vertical line at 500 m distance from the injection well: DARSim (red) and other benchmark groups (black).

Figure 6B shows the CO2 saturation profile at 500 meters from injection well after 2 years. Result obtained from DARSim agrees well with those reported in literature. CO2 saturation gradually increases along the elevation within a CO2 plume. However, there is an abrupt decrease of CO2 saturation to around 0.1 at the interfaces of sand and shale layers. CO2 in the bottom of sand layers have a similar saturation as in shale layers. The highest CO2 plume is missing in the profile plot of the vertical line because the plume did not migrate to 500 meters after 2 years.

Validation of corner-point grids implementation

This test case is designed to evaluate the reliability of the extension of compositional framework to corner-point grids by comparing the simulation results on Cartesian grids and converted corner-point grids. The geometry information of corner-point grids is generated based on the open-source simulator MRST (Ding et al., 1995; Lie et al., 2019; HosseiniMehr et al., 2022).

The aquifer is modelled by a two-dimensional vertical cross section as shown in Figure 7, which has a length of 200 meters and height of 50 meters. The aquifer is discretized by 200 × 50 cells to have a grid resolution of 1 meter by 1 meter. An injection well is placed at the bottom 10 meters of left boundary, and the whole 50 meters at the right boundary is perforated for a production well. CO2 is injected into the aquifer at a rate of 8×10^{-5} pore volume per day for 600 days, and total time of 36000 days are simulated. The depth of the aquifer is set to be deeper than 2500 meters to represent the typical CO2 sequestration targets. Several physical parameters used in the simulation, such as initial pressure and temperature, are summarized in Table 2 (Ide et al., 2007; Wang et al., 2022). The relative permeability and capillary pressure curves presented in chapter 3 are used during simulation.

Table 2—Physical parameters and simulation settings of the 2D cartesian box test case

Properties	Symbols	Values	Units
Reservoir length	L	100	m
Reservoir height	H	50	m
Porosity	ϕ	0.2	–
Permeability	k	40	mD
Initial reservoir pressure	p_0	2.5e7	Pa
Bottom hole pressure	p_w	2.5e7	Pa
Reservoir temperature	T	338.15	K
CO2 density at STC	ρ_{CO2}^{STC}	1.98	kg/m^3
Brine density at STC	ρ_b^{STC}	1060	kg/m^3
Brine salinity	–	1.0e5	ppm
Injection rate	q	8.0$e-5$	PV/day
Injection time	t_{inj}	600	day
Simulation time	t_{tot}	36000	day

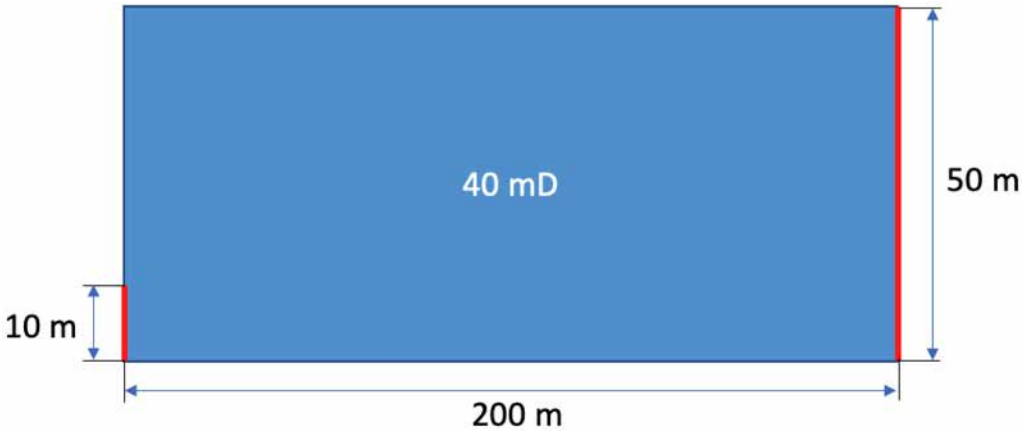

Figure 7—Setup of the 2D cartesian box model

At the end of simulation, the evolution of CO2 plume at nondimensionalized elapsed time and quantitative trapping amount by different mechanisms are obtained. The dissolution and residual trapping are quantified by the solution CO2-brine ratio and saturation map respectively. An overall trapping amount is determined with summation of the two, because they are normally regarded as securely trapped part in hydrodynamic trapping, which is the collective term for structural, dissolution and residual trapping. All those trapping amounts are expressed in scaled total injected amount of CO2 in the reservoir, or the fraction of injected CO2.

The simulation results of Cartesian grids and converted corner-point grids are presented in Figure 8 side by side. The evolution of gas saturation on cartesian and corner-point grids is very similar, while the solution CO2-brine ratio maps show some small differences in fingering behaviors during post-injection period. However, it is mainly resulted from the sensitivity of fingering behavior to the perturbation at the interface, instead of wrong treatment during extension to corner-point grids.

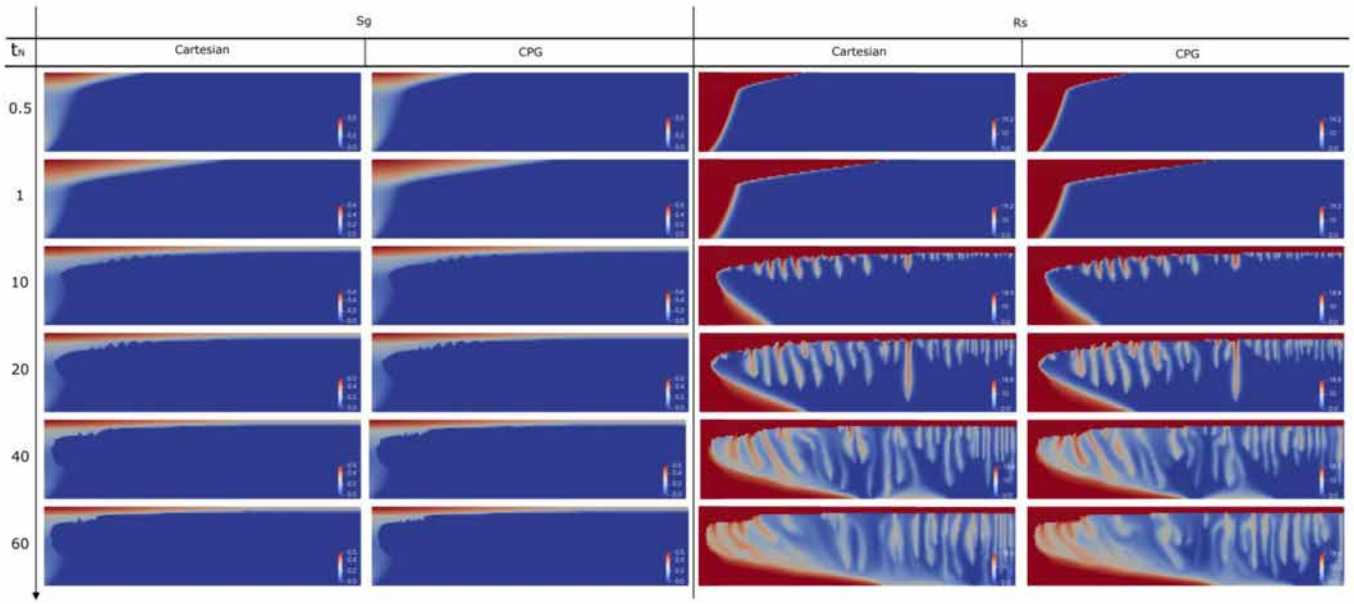

Figure 8—Comparison of simulation results of gas saturation (left) and solution CO2-brine ratio (right) on cartesian and corner-point grids.

The time-lapsed behaviors of different trapping mechanisms on two types of reservoir grid are also compared quantitively in terms of trapping amount. Figure 9 shows the predicted trapping amount due to dissolution, residual trapping and their combination, on corner-point grids agree well with the prediction

from Cartesian grids. Specifically, the dissolution trapping undergoes a substantial growth during injection period. After that, the growth of dissolution slows down and then shows an even larger increase rate at the end of post-injection. In contrary, only small amount of CO2 get residual trapped during injection period, and there is an abrupt increase after injection stops. However, residual trapping amount starts decrease after it reaches its maximum during post-injection.

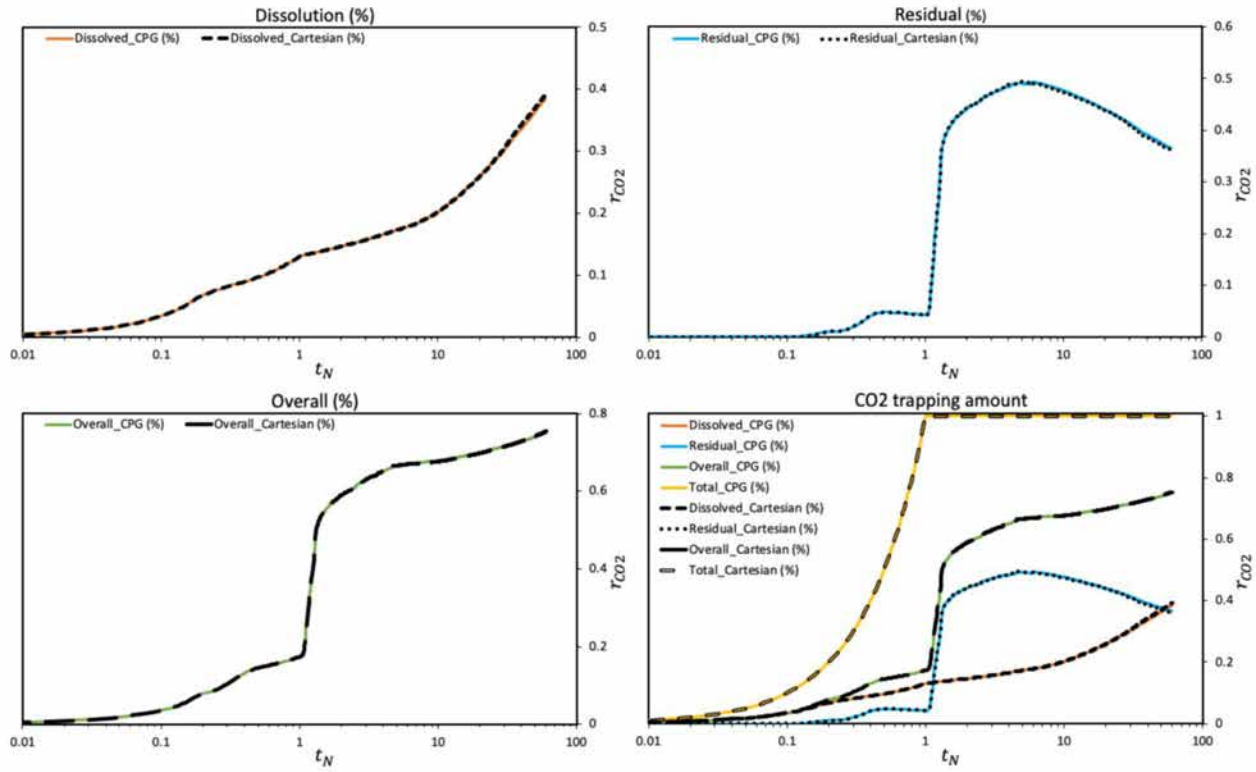

Figure 9—Fraction of injected CO2 trapped by different mechanisms on cartesian and corner-point grids of the 2D cartesian box model.

Simulation of CO2 storage in Johansen field

Model description

The Johansen formation is a deep saline aquifer of the Sognefjord delta, located about 60 km west of Mongstad area at the south-western coast of Norway, as shown by the geographic map in Figure 10A (Eigestad et al., 2009). It is located at depth from 2200 to 3100 m below sea level and belongs to the lower Jurassic Dunlin Gp. The formation spreads 60 to 100 km in lateral direction, with an average thickness of 100 meters. As for neighboring geological layers, the Johansen formation is overlaid by thick Dunlin shale in most investigating area, and it immediately lies above the Amundsen shale (Class et al., 2009).

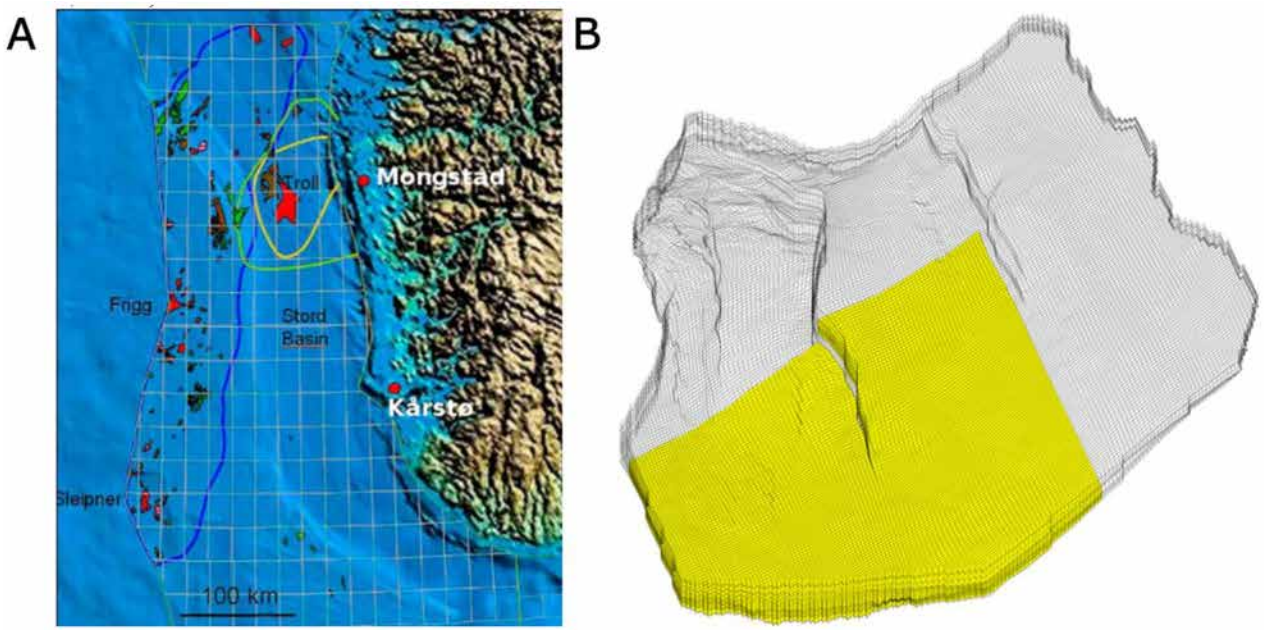

Figure 10—Location of Johansen field. (A) Geographic location. (B) Sector model location.The Johansen dataset, based on available seismic and more than 12 well logs in the MatMoRA project (Eigestad et al., 2009), provides an excellent calibration tool for modelling CO2 flow and transport in field scale. The full field model covers all zones and the entire lateral domain mentioned above, consisting of 149 × 189 × 16 grid cell. In this study, the heterogeneous sector model in Figure 10B, discretizing the southwestern part of the geological domain with 100 × 100 × 11 grid cells, is used. As shown by Figure 11, the porosity of Johansen formation is populated with a porosity-depth trend obtained from a neighboring field at equivalent depth level. The permeability values are modelled on a basis of porosity-permeability trend depending on the Sognerfjord formation analogue. The permeabilities in x and y direction are assumed to be the same, while the vertical permeability is ten times smaller than horizontal permeability. The fluid properties together with some physical parameters used in the following simulations are summarized in Table 3.

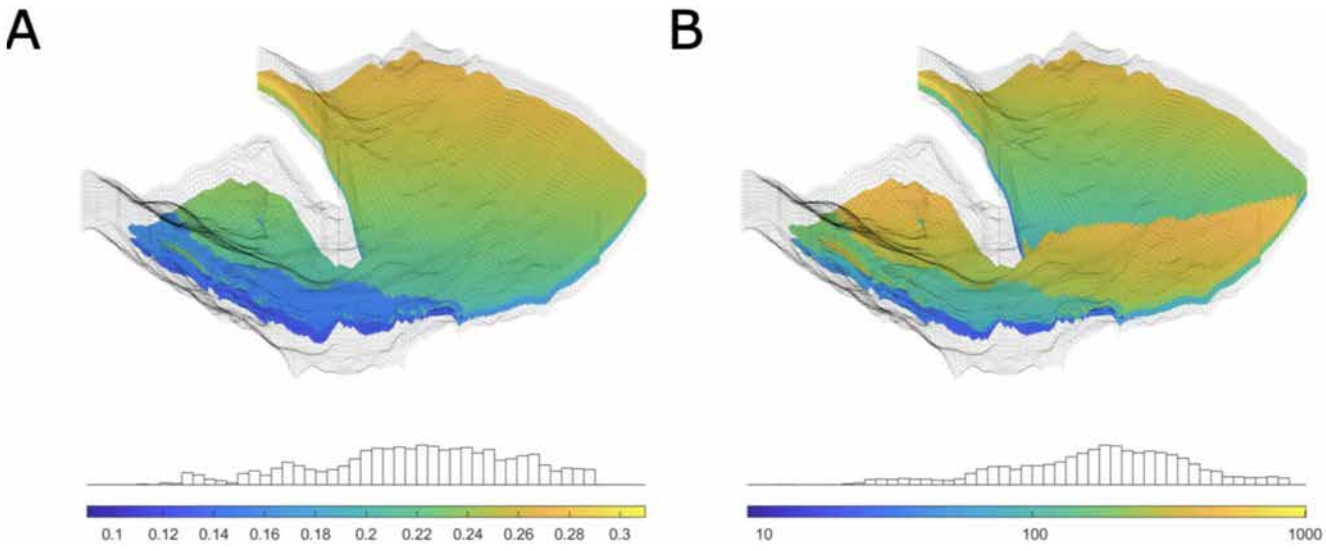

Figure 11—Distribution of porosity (A) and permeability (B) in Johansen formation, with sector model outlined by wireframe.

Table 3—Physical parameters and simulation scheme of the Johansen test case.

Parameter	Value	Unit
Reservoir temperature	94	°C
Initial reservoir pressure @3100m	310	*bar*
CO2 viscosity @ 280 bar	5.65e − 5	*Pa.s*
Brine viscosity @ 280 bar	3.88e − 4	*Pa.s*
Injection rate	4	*Mt/year*
Injection time	100	*year*
Simulation time	2000	*year*

We assume a No-flow boundary condition, in which the top and bottom boundaries are set impermeable to represent the bounding shale layers above and below. There is no flow happening across lateral boundaries, so the injected CO2 stays in the domain if it reaches the boundaries. A production well is perforated at north-eastern corner to avoid overpressurizing the domain. The injection well is placed at the south-west direction to the major north-south trending fault, which is the deeper part of the domain (Afanasyev 2013). The well pattern used during simulations are given by Figure 12.

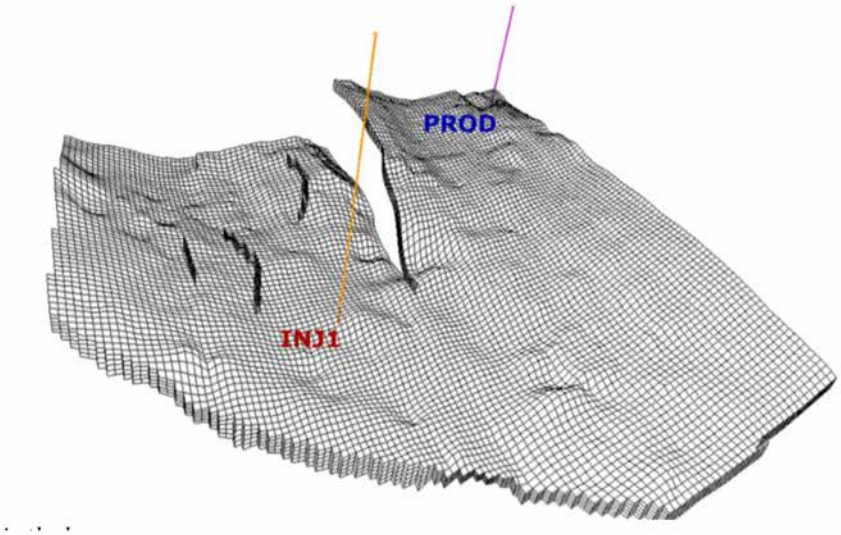

Figure 12—Well pattern in the base case.

Assuming a geothermal gradient of 3 °C per 100m, the reservoir temperature is assumed to be constant at 94 °C with a surface temperature of 10 °C. The initial pressure in the reservoir is determined by hydrostatic distribution, with a pressure value of 310 bar at reference depth 3100m. Eigestad et al. (2009) suggested that CO2 can be injected at a rate of 4 Mt per year to demonstrate the storage capacity of Johansen formation. In this work, 400 Mt of CO2 is injected into the reservoir over 100 years, after which both injection and production well are shut down. After injection ceases, the simulation continues until 2000 years to predict the migration of CO2 plume and trapping amount during post-injection period.

Impacts of different physics

The proposed compositional framework incorporates dissolution, hysteresis and capillarity, which are believed to be important for CO2 trapping in saline aquifers. However, to evaluate the relative importance of those physics and better understand the roles they are playing in trapping CO2, a set of simulations in the absence of different physics are compared against the base case, which includes all physics.

The CO2 saturation profiles at different time steps are given in Figure 13. Firstly, the base case results are used here to illustrate the evolution of saturation distribution. Since the injection well is placed in the most deep-seated region, CO2 starts to flow upward and does not migrate very far in the lateral direction because of the strong buoyancy force. The upward CO2 plume soon is hindered by the top boundary and spread out in the top layers. At the end of CO2 injection, the plume front reaches the east part of domain and tends to migrate to north-east direction further due to the structure dip trend. Dominated by the advective force during injection, the saturation behind the front is relative constant no matter how the depth varies in the top layer. However, only some local domes are filled with high saturation of CO2 after injection stops, because dominating buoyancy force drives part of the CO2 at low regions to migrate further to northeast direction. At some point before 2000 years, the CO2 plume reaches the eastern boundaries of the domain and is accumulated at those locations.

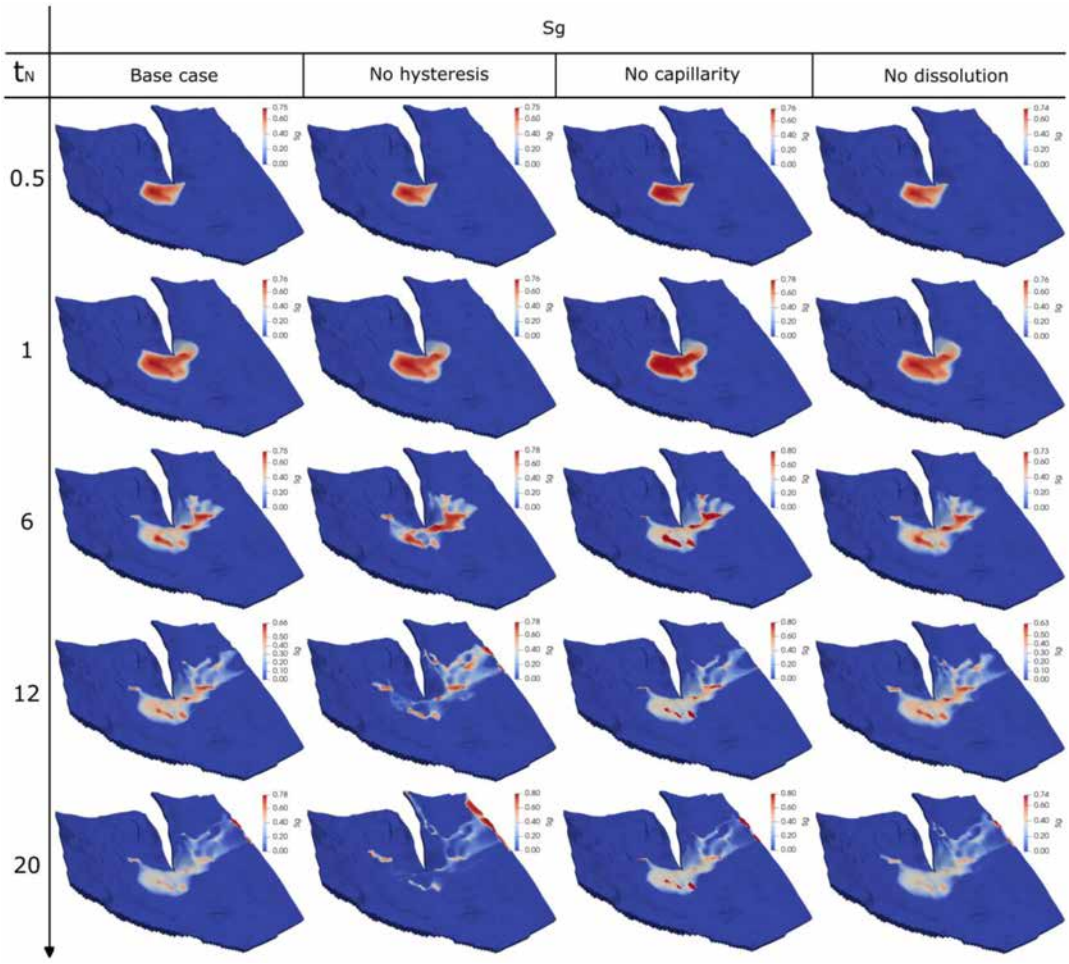

Figure 13—Gas saturation profiles for various scenarios in the Johansen field. (Base case includes all physical effects).

By neglecting the hysteresis behavior, the same primary drainage curves are used to evaluate constitutive relations during drainage and imbibition process. It indicates the residual gas saturation is zero, or gas saturation can decrease to zero during imbibition. During injection period, saturation profiles do not show much difference from the base case because mostly drainage process occurs to the reservoir. The largest difference during post-injection period is gas saturation in most low regions decreases to zero, and only some local peaks in the migration path are filled with CO2. Because more CO2 is free to migrate to the east half from deep regions, the CO2 plume sweeps more areas and even reaches the fault boundary. In addition, the maximum of CO2 saturation occurring to the accumulation areas is larger due to the same behavior.

Following that, we exclude the capillary pressure by equating the pressure in different phases. During injection period, the only obvious difference is the maximum saturation within the plume is slightly larger. However, sharper interfaces between local domes saturated with CO2 and lower regions are observed during post-injection. Thus, it can inferred that capillarity can help the imbibition of brine into CO2 plume, and form a transition zone.

When neglecting dissolution, we assume that CO2 only exist in gas phase and the compositional flow is simplified to immiscible two-phase flow. In consequence, the solution ratio maps are missing in Figure 14, because the amount of dissolution trapping remains zero. As shown by the outline of CO2 plume, the plume front without dissolution propagates further than its counterpart in base case, due to the increase of free CO2 in the absence of dissolution.

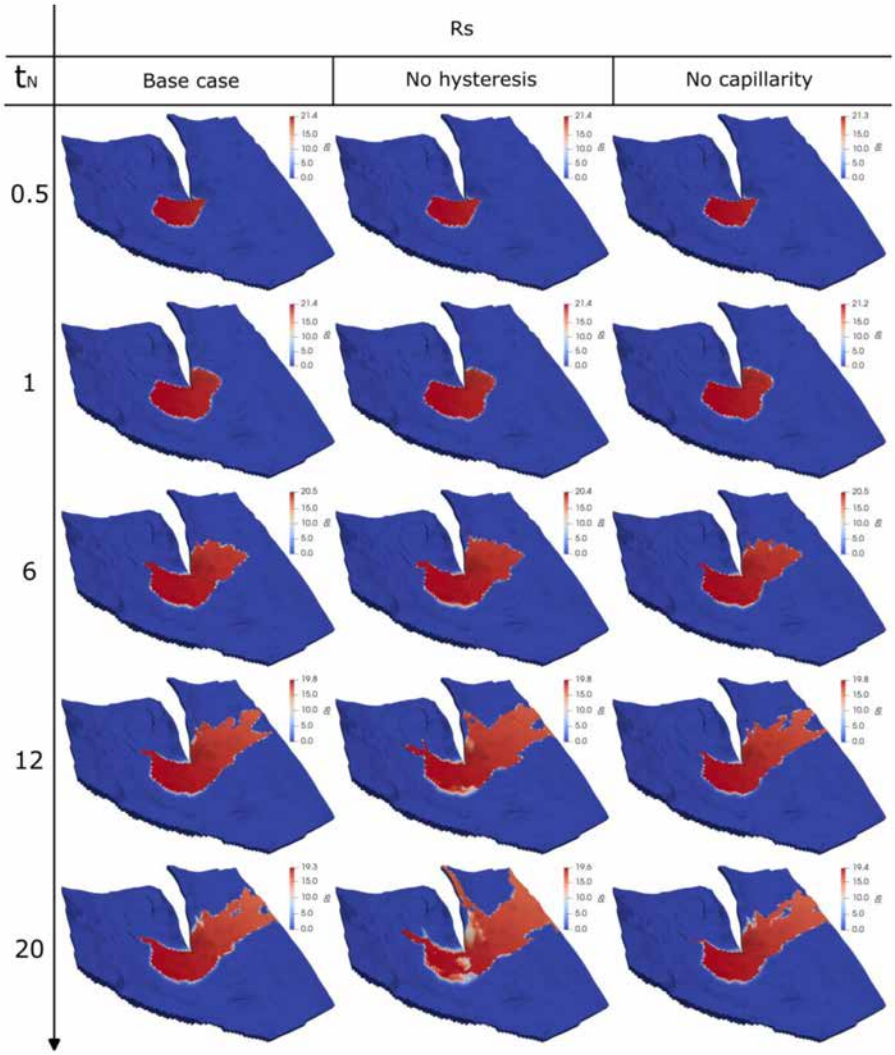

Figure 14—Solution CO2-brine ratio profiles for various scenarios in the Johansen field. (No dissolution test case is missing because the solution ratio is always zeros.)

Figure 14 shows the dissolution ratio maps at five moments in the absence of different physics. It is clearly revealed that the dissolution happens along the invasion of CO2 plume by base case results, while the dissolution front is slightly ahead than the plume front in the saturation plot. In addition, it is noted that the solution ratio values gradually decrease as it moves to the eastern boundary since the dissolution limit has a dependency on pressure. In the absence of hysteresis, more cells, particularly cells along the fault

boundary, are swept by dissolved CO2 because more CO2 are in mobile state, instead of in residual form. However, neglecting capillarity does not have a big impact on the distribution of solution ratio.

Figure 15 shows the fraction curves of trapping amount, and it clearly reveals the different time scales on which various trapping mechanisms act. During the injection period, the rate of the amount of CO2 dissolved in brine gradually increase, while it slows down immediately after injection stops and increases again after some time. However, it is obvious that dissolution plays an equally important role during injection and post-injection periods. On the other hand, the residual trapping amount starts rising rapidly after the cease of injection, until a majority of CO2 is in residual form before the decrease around 1000 years. The fraction curves of overall trapping indicate the structural trapping plays a decreasing role while the residual and solubility trapping become more important along time.

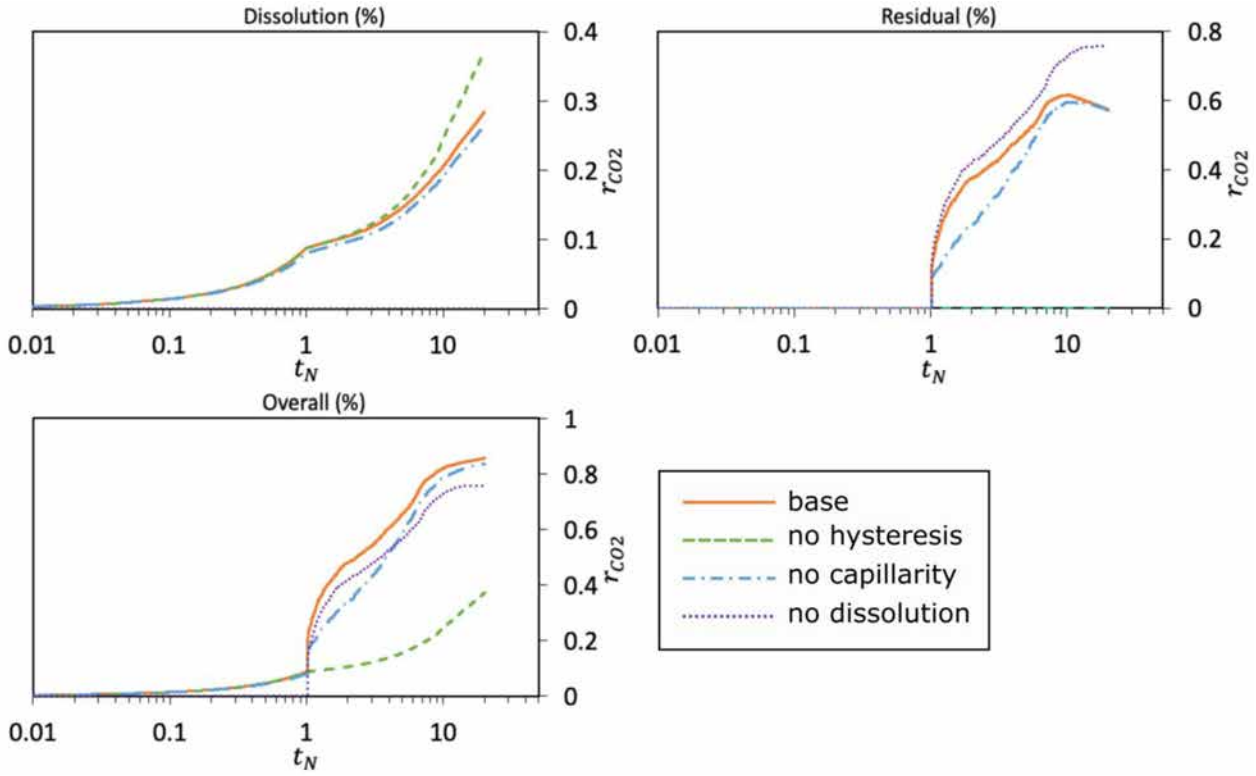

Figure 15—Fraction of injected CO2 trapped by different mechanisms for various scenarios in the Johansen test case.

In the case of no dissolution, the amount of residual trapping also increases rapidly after injection stops. One important difference is that the maximum fraction it reaches is even larger than that of the base case. The larger fraction value is caused by the further front position of CO2 plume in the absence of dissolution, and a larger swept area. On the other hand, residual trapping amount remains constant afterwards, because residually trapped gas cannot be dissolved by the convective fingering as the base case.

When removing capillarity, the amount of dissolution trapping agrees well with base case during injection, except a minor deviation of starting from $t_N = 0.2$. This deviation causes a slightly smaller fraction of CO2 dissolved in brine at the end. It is because higher saturations in invading zone lead to a smaller swept area. The dynamic change of residual trapping amount shows a similar pattern as the base case, which can prove that an interplay between hysteresis and dissolution trapping exists. However, a slower decreasing rate is observed at the end. It can be inferred that the convective transport during postinjection is impacted by the balance between capillary and buoyancy force. The existence of capillary pressure can help brine be imbibed into top gas cap, and CO2 can leave the top layer in the form of descending fingers.

In the absence of hysteresis, the amount of CO2 in residual form is zero all the time because residual gas saturation decreases to zero. The amount of dissolved CO2 during injection does not show much difference from the base case, while a significant larger fraction of CO2 is trapped in dissolution form during post-injection period. This difference is resulted from a larger swept area without residual trapped CO2.

Conclusion

In this work, we present a compositional model that is developed to simulate CO2 storage in saline aquifers with complex geological formations based on corner-point grid geometries. Essential trapping mechanisms are accounted for in a unified framework. Particularly, a parameterization method is proposed to describe hysteretic effect in constitutive relations. The developed numerical model is validated by comparing simulation results reported in literature, as well as those obtained in Cartesian grids. A field-scale study is performed to investigate the roles played by various physics in CO2 trapping.

Results show that the dissolution of CO2 in brine occurs when CO2 and brine are in contact. As CO2 migrates and spreads in top layer, the brine dissolved with CO2 sits on the top of pure brine, which leads to gravitational instability. Eventually, this would trigger the convective transport from plume above to the bottom of aquifer. On the other hand, the hysteresis behavior of constitutive relations, or their dependency on saturation history, are captured by proposed scanning curve surfaces robustly. The unique residual saturation and capillary pressure of every cell, depending on their own saturation history, can be modelled. They can have an important impact on the migration of CO2 plume and swept areas, through which the dissolution and residual trapping amount are affected.

The fraction curves of trapping amount by various mechanisms indicate that identified trapping mechanisms operate on a variety of time scales. In particular, the increase rate of dissolution trapping amount often changes after injection stops, but the trapping contribution is found equally important during injection and post-injection period. On the contrary, residual trapping often starts playing a role after injection stops, while its contribution can surpass that of dissolution trapping in a short time. At the late stage, obvious evidence shows that the two trapping mechanisms interact with each other and causes a decrease of the trapping amount in residual form.

Acknowledgments

We thank group members of DARSim (Delft Advanced Reservoir Simulation) and ADMIRE (Adaptive Dynamic Multiscale Integrated Reservoir Earth) for discussions during the development of this work. The author also acknowledges the financial support of China Scholarship Council (No. 202207720047).

References

Afanasyev, A., Kempka, T., Kuhn, M., and Melnik, O. 2016. Validation of the MUFITS reservoir simulator against standard CO2 storage benchmarks and history-matched modelsof the ketzin pilot site. *Energy Procedia* **97**, 395–402.

Afanasyev, A. A. 2013. Application of the reservoir simulator MUFITS for 3d modelling of CO2 storage in geological formations. *Energy Procedia* **40**, 365–374.

Class, H., Ebigbo, A., Helmig, R., Dahle, H. K., Nordbotten, J. M., Celia, M. A., Audigane, P., Darcis, M., Ennis-King, J., Fan, Y., Flemisch, B., Gasda, S. E., Jin, M., Krug, S., Labregere, D., Beni, A. N., Pawar, R. J., Sbai, A., Thomas, S. G., Trenty, L., and Wei, L. 2009. A benchmark study on problems related to CO2 storage in geologicformations. *Computational Geosciences* **13**, 4, 409–434.

Cooper, C. 2009. A technical basis for carbon dioxide storage. *Energy Procedia* **1**, 1, 1727–1733.

Cusini, M., Fryer, B., van Kruijsdijk, C., and Hajibeygi, H. 2018. Algebraic dynamic multilevel method for compositional flow in heterogeneous porous media. *Journal of Computational Physics* **354**, 593–612.

Ding, Y., and Lemonnier, P. 1995. Use of corner-point geometry in reservoir simulation. SPE-29933-MS.

Duan, Z., and Sun, R. 2003. An improved model calculating CO2 solubility in pure waterand aqueous NaCl solutions from 273 to 533 k and from 0 to 2000 bar. *Chemical Geology* **193**, 3-4, 257–271.

Eigestad, G. T., Dahle, H. K., Hellevang, B., Riis, F., Johansen, W. T., and Øian, E. 2009. Geological modeling and simulation of CO2 injection in the johansen formation. *Computational Geosciences* **13**, 4, 435–450.

Elenius, M., Voskov, D., and Tchelepi, H. 2015. Interactions between gravity currents andconvective dissolution. *Advances in Water Resources* **83**, 77–88.

Emami-Meybodi, H., Hassanzadeh, H., Green, C. P., and Ennis-King, J. 2015. Convectivedissolution of CO2 in saline aquifers: Progress in modeling and experiments. *International Journal of Greenhouse Gas Control* **40**, 238–266.

Fanchi, J. R. 2002. Shared Earth Modeling. Elsevier.

Hajibeygi, H., and Tchelepi, H. A. 2013. Compositional multiscale finite-volume formulation. *SPE Journal* **19**, 02, 316–326.

Hassanzadeh, H., Pooladi-Darvish, M., Elsharkawy, A. M., Keith, D. W., and Leonenko, Y. 2008. Predicting PVT data for CO2–brine mixtures for black-oil simulation of CO2geological storage. *International Journal of Greenhouse Gas Control* **2**, 1, 65–77.

Hermanrud, C., Andresen, T., Eiken, O., Hansen, H., Janbu, A., Lippard, J., Boloas, H. N., Simmenes, T. H., Teige, G. M. G., and Østmo, S. 2009. Storage of CO2 in salineaquifers–lessons learned from 10 years of injection into the utsira formation in thesleipner area. *Energy Procedia* **1**, 1, 1997–2004.

HosseiniMehr, M., Tomala, J. P., Vuik, C., Kobaisi, M. A., and Hajibeygi, H. 2022. Projection-basedembedded discrete fracture model (pEDFM) for flow and heat transfer in real-field geological formations with hexahedral corner-point gridss. *Advances in Water Resources* **159**, 104091.

Ide, S. T., Jessen, K., and Orr, F. M. 2007. Storage of CO2 in saline aquifers: Effects of gravity, viscous, and capillary forces on amount and timing of trapping. *International Journal of Greenhouse Gas Control* **1**, 4, 481–491.

Juanes, R., Spiteri, E. J., Orr, F. M., and Blunt, M. J. 2006. Impact of relative permeabilityhysteresis on geological COsub2/ substorage. *Water Resources Research* **42**, 12.

Killough, J. 1976. Reservoir simulation with history-dependent saturation functions. *Societyof Petroleum Engineers Journal* **16**, 01, 37–48.

Lie, K. A. 2019. An Introduction to Reservoir Simulation Using MATLAB/GNU Octave: UserGuide for the MATLAB Simulation Toolbox (MRST). Cambridge University Press.

Lyu, X., Voskov, D. V., and Rossen, W. R. 2021. Numerical investigations of foam-assisted CO2 storage in saline aquifers, *International Journal of Greenhouse Gas Control*, **108**, 103314.

Metz, B., Davidson, O., De Coninck, H., Loos, M., and Meyer, L. 2005. IPCC special reporton carbon dioxide capture and storage. Cambridge: Cambridge University Press.

Oak, M., Baker, L., and Thomas, D. 1990. Three-phase relative permeability of Berea sandstone. *Journal of Petroleum Technology* **42**, 08, 1054–1061.

Pini, R., and Benson, S.M. 2017. Capillary pressure heterogeneity and hysteresis for the supercritical CO2/water system in a sandstone. *Advances in Water Resources*, **108**, 277–292.

Pruess, K., Garcia, J., Kovscek, T., Oldenburg, C., Rutqvist, J., Steefel, C., and Xu, T. 2004. Code intercomparison builds confidence in numerical simulation models for geologicdisposal of CO2. *Energy* **29**, 9-10, 1431–1444.

Shao, Q., Matthai, S., Driesner, T., and Gross, L. 2020. Predicting plume spreading during CO2 geosequestration: benchmarking a new hybrid finite element–finite volumecompositional simulator with asynchronous time marching. *Computational Geosciences* **25**, 1, 299–323.

Spycher, N., and Pruess, K. 2005. CO2-H2O mixtures in the geological sequestration of CO2. II. partitioning in chloride brines at 12–100°c and up to 600 bar. *Geochimica etCosmochimica Acta* **69**, 13, 3309–3320.

Spycher, N., Pruess, K., and Ennis-King, J. 2003. CO2-h2o mixtures in the geological sequestration of CO2. i. assessment and calculation of mutual solubilities from 12 to 100°cand up to 600 bar. *Geochimica et Cosmochimica Acta* **67**, 16, 3015–3031.

Voskov, D. V., and Tchelepi, H. A. 2012. Comparison of nonlinear formulations for two-phase multi-component EoS based simulation. *Journal of Petroleum Science and Engineering* **82-83**, 101–111.

Wang, Y., Vuik, C., and Hajibeygi, H. 2022. Analysis of hydrodynamic trapping interactionsduring full-cycle injection and migration of CO2 in deep saline aquifers. *Advances in Water Resources* **159**, 104073.

Wang, Y., Vuik, C., and Hajibeygi, H. 2022. CO2 storage in deep saline aquifers: impacts of fractures on hydrodynamic trapping. *International Journal of Greenhouse Gas Control* **113**, 103552.